A numerical investigation of isobaric combustion strategy in a compression ignition engine

Xinlei Liu[1,*], Hammam Aljabri[1], Balaji Mohan[1], Rafig Babayev[1],

Jihad Badra[2], Bengt Johansson[1], Hong G. Im[1]

[1] Clean Combustion Research Center (CCRC), King Abdullah University of Science and Technology (KAUST), Thuwal, Saudi Arabia

[2] Fuel Technology Division, R&DC, Saudi Aramco, Dhahran, Saudi Arabia

*Corresponding author: Xinlei Liu; Email: xinlei.liu@kaust.edu.sa

Abstract

Three-dimensional computational fluid dynamic simulations were conducted to study the means to achieve isobaric combustion mode in a compression ignition engine, which is intended to be used in the high-efficiency double compression-expansion engine (DCEE) concept. Compared to the conventional diesel combustion mode, the isobaric combustion mode generated a significantly lower peak combustion pressure, which was beneficial for the high load extension. For both combustion modes, the ignition was triggered downstream of the nozzle, with the heat release dominated by $HCO+O_2=CO+HO_2$, while the injection-combustion duration for the isobaric combustion mode was significantly longer. The effects of swirl ratio, spray angle, and piston geometries on the isobaric combustion at various engine loads were also investigated. The higher swirl ratio resulted in a higher heat transfer loss and thus lower thermal efficiency. Due to the higher air utilization rates and lower heat transfer losses, cases with spray angles of 140° and 150° generated the higher thermal efficiencies. The piston bowl geometry was found to have a significant impact on the mixing and combustion processes, especially at high engine load conditions. For the conditions under study, the original piston geometry with a swirl ratio of 0 and a spray angle of 140° demonstrated the highest thermal efficiency

for the isobaric combustion mode. The results of this work will provide guidance in the practical design and implementation of the DCEE concept.

Keywords: Isobaric combustion; Compression ignition; Double compression expansion engine; Thermal efficiency; Diesel

Nomenclature

AMR	Adaptive mesh refinement	LP	Low-pressure
C_2H_4	Ethylene	LTC	Low-temperature combustion
CA ATDC	Crank angle after the top dead center	NOx	Nitric oxides
CAC	Charge air cooler	PCCI	Premixed charge compression ignition
CDC	Conventional diesel combustion	ϕ	Equivalence ratio
CFD	Computational fluid dynamics	REXR	Representative exothermic reaction
CI	Compression ignition	ROI	Rate of injection
CO	Carbon monoxide	PPC	Partially premixed combustion
CR	Compression ratio	SA	Spray angle
DCEE	Double compression expansion engine	SI	Spark ignition
DI	Direct injection	SOI	Start of injection
EGR	Exhaust gas recirculation	SW	Swirl ratio
EVO	Exhaust valve opening	T	Temperature
GHG	Greenhouse gas	TDC	Top dead center
HP	High-pressure	THC	Total hydrocarbon
HRR	Heat release rate	TKE	Turbulent kinetic energy
HTR	Heat transfer rate	1D	One-dimensional
ICE	Internal combustion engine	3D	Three-dimensional
IVC	Intake valve closing		

1. Introduction

The greenhouse gas (GHG) emissions from the utilization of petroleum-derived fuels are a major concern for regulatory authorities, who are enforcing stringent CO_2 and tailpipe emission regulations on the transportation sector. To fulfill the stringent CO_2 targets, the engine fuel economy, and hence, the thermal efficiency of internal combustion engines (ICE) need to be further improved [1-3].

Compared to the spark ignition (SI) engines whose compression ratio (CR) is limited by the knocking issue and the intake throttle losses [4], the compression ignition (CI) engines can achieve higher CR and efficiencies by employing non-premixed combustion using direct injection (DI) strategies with variable injection timing. While the maximum CR is limited by the material, some large marine engines operate at CR higher than 20, which extends their indicated thermal efficiency up to 55% [5]. For land-use engines, however, it is too heavy and expensive to adopt such a large-size engine setup. As such, improvements in thermal efficiency require systematic optimization in order to minimize various losses associated with gas exchange, combustion, heat transfer, and mechanical friction [6, 7], along with the reduction of pollutant emissions like nitric oxides (NOx) and soot [8, 9]. Over the past decades, various advanced combustion strategies were proposed, including the homogeneous charge compression ignition (HCCI) [9], the premixed charge compression ignition (PCCI) [10], and partially premixed combustion (PPC) [11, 12], all of which aim to achieve higher efficiency and lower emissions. In fact, the HCCI, PCCI, and PPC concepts all belong to the category of low-temperature combustion (LTC), which adopts exhaust gas recirculation (EGR) to control the combustion process [13-16]. The primary difference for these three concepts is the different start of injection (SOI) timings, which will lead to the different levels of charge stratification accordingly.

Considering that the CR is the primary factor that increases the thermodynamic efficiency, Lam et al. [5] recently proposed the double compression expansion engine (DCEE) concept, which adopts two-stage compression and expansion processes to achieve high thermal efficiency at a wider range of operating conditions and more flexibility in optimization strategies. Figure 1 illustrates a schematic of the DCEE concept [5]. It consists of two 4-stroke machines, a large-size low-pressure (LP) unit, and a small-size high-pressure (HP) unit. The LP unit performs two tasks: 1. it inducts fresh air, compresses it (for the first time), and transfers through the charge air cooler (CAC) into the HP unit; 2. it receives exhaust gas of the HP unit and performs the second expansion stage before discharging the gas into the atmosphere. The HP unit is essentially a combustion cylinder of a conventional diesel engine, where fresh air is compressed (for the second time) and combustion products and expanded (for the first time). Due to the small size of the HP unit, heat transfer and friction losses are both minimized. A one-dimensional (1D) modeling study revealed that the DCEE concept could potentially achieve brake thermal efficiency of 56 % [17].

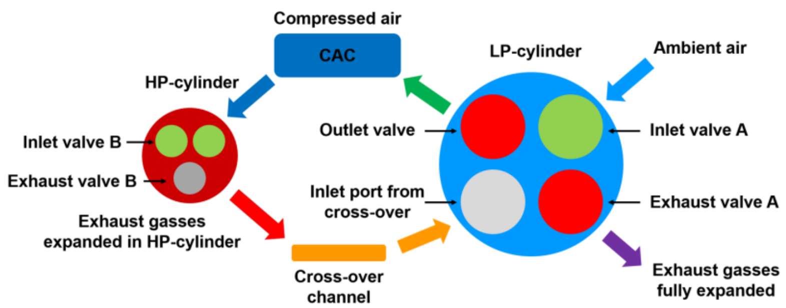

Fig. 1. *Schematic of the DCEE concept [5].*

Owing to the excessive pressure (up to 300 bar) in the HP unit, it is desirable for the DCEE concept to adopt an isobaric combustion strategy instead of a typically preferred isochoric combustion strategy [18, 19]. Okamoto and Uchida's work [20] has shown that it is possible to realize isobaric combustion using three injectors. More recently, Babayev et al. [21] reported that the isobaric combustion could be achieved using only a single high-pressure injector with multiple injection events. They also compared the combustion performance of the CDC mode and isobaric combustion mode, which demonstrated comparable thermal efficiencies. Note that the peak combustion pressure for the CDC mode was significantly higher than the isobaric combustion mode, suggesting lower friction losses for the latter.

The previous studies related to the isobaric combustion strategy are mostly focused on experimental or 1D simulation research [5, 18]. Therefore, this work intends to further enhance our understanding of the isobaric combustion strategy using the three-dimensional (3D) computational dynamics fluid (CFD) approach. A data-processing method developed by Liu et al. [22, 23] was also adopted to compare the different heat release features of the isobaric and CDC combustion modes. Following that, the effects of some significant engine design parameters, including swirl ratio, spray angle, and piston geometries, on engine combustion performance and emissions at various engine load conditions were investigated. This work will provide valuable guidance for the future development of the practical applications of the DCEE concept.

2. Experimental and modeling setup

2.1. Experimental setup

Experimental work was performed by Babayev et al. [18] on a modified single-cylinder diesel engine. Figure 2 depicts the schematic of the engine setup and Table 1 lists the engine specifications and operating conditions [18]. Detailed descriptions of the engine setup can be found in [18, 21]. During the experiment, the engine speed was kept at 1200 rpm. The intake pressure and temperature were fixed at about 3.1 bar and 353 K, respectively. A solenoid-valve common-rail injector was used for fuel injections with an injection pressure of 2300 bar. For the isobaric combustion mode, the target was to achieve a constant compression pressure of 150 bar, due to limitations of the air-intake system. Four different injection strategies involving 2 to 5 injection events were tested, corresponding to the different engine load conditions. For comparison, a CDC case was also tested under the engine load similar to the 4-injection case. Table 2 shows the detailed information of the injected mass and the SOI timings. The rate of injection (ROI) was measured by Babayev et al. [18] using a novel in-situ measurement technique. The results are shown in Fig. 3, which were adopted as input parameters for the engine combustion simulations.

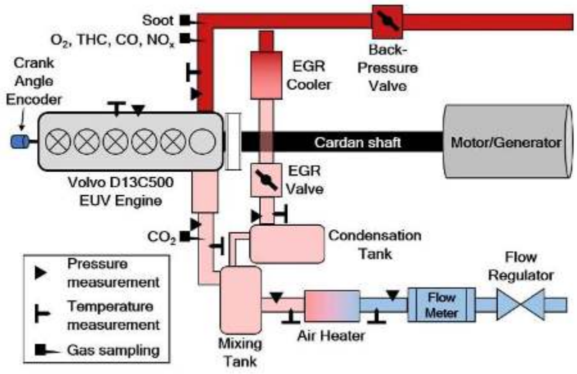

Fig. 2. *Schematic of* the engine *setup [18].*

Table 1. *Engine specification and operating condition.*

Engine configuration	Single-cylinder, water-cooled
Number of valves	4
Bore/stroke (mm)	131/158
Connecting rod length (mm)	255
Displacement volume (L)	2.13
Geometric compression ratio	17:1
Swirl ratio	0
Intake valve close timing (° CA ATDC)	-160
Exhaust valve open timing (° CA ATDC)	140
Common-rail injector	7 holes, injection angle 150°, 0.225 mm nozzle
Engine speed (rpm)	1200
Intake air pressure (bar)	3.1
Intake air temperature (K)	353
EGR ratio (%)	0

Table 2. *Injection details [18].*

	2 inj.	3 inj.	4 inj.	5 inj.	CDC
Total injected mass (mg/cycle)	20.7	64.7	117.6	222.0	119.1
IMEP (bar)	1.3	5.9	11.1	19.7	11.3
SOI/Dur. 1st inj. (° CA ATDC)	-3.0/2.4	-3.0/2.4	-3.0/2.4	-3.0/2.4	-1.5/8.4
SOI/Dur. 2nd inj. (° CA ATDC)	0.5/2.4	0.5/2.6	0.5/2.2	0.5/2.4	-
SOI/Dur. 3rd inj. (° CA ATDC)	-	4.5/3.4	4.5/3.4	4.5/3.2	-
SOI/Dur. 4th inj. (° CA ATDC)	-	-	9.0/4.4	9.0/10.4[a]	-
SOI/Dur. 5th inj. (° CA ATDC)	-	-	-	12.7/10.4[a]	-

[a] Denotes the total duration for the 4th and 5th injections.

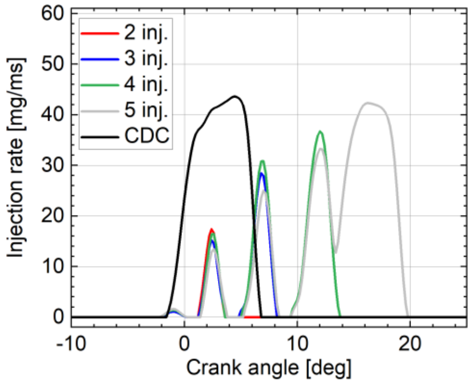

Fig. 3. *Measured ROI profiles [18].*

2.2. Computational setup

2.2.1. Spray and combustion models

The 3D CFD modeling study was performed using the CONVERGE 2.4 package [24]. A Lagrangian-parcel method was utilized to describe the liquid spray dynamics [25]. The Kelvin-Helmholtz Rayleigh-Taylor model without a breakup length was adopted to predict the droplet breakup [26], the no-time-counter algorithm was adopted to predict the droplet collision [27], and the Frossling correlation approach was used to simulate droplet evaporation [28]. The SAGE detailed chemical kinetics solver [29] coupled with the reduced n-heptane mechanism developed by Wang et al. [30] was adopted for the diesel combustion simulation. Detailed descriptions of these modules can be found in [31].

2.2.2. Turbulence model

The renormalization group k-ε model was utilized to simulate the turbulence [32]. The modeled Reynolds stress is given by,

$$\tau_{ij} = -\bar{\rho}\widetilde{u_i' u_j'} = 2\mu_t S_{ij} - \frac{2}{3}\delta_{ij}\left(\rho k + \mu_t \frac{\partial \widetilde{\mu_i}}{\partial \widetilde{x_i}}\right) \qquad (1)$$

in which the turbulent kinetic energy, turbulent viscosity, and mean strain rate tensor are respectively defined as,

$$k = \frac{1}{2}\widetilde{u_i' u_i'} \tag{2}$$

$$\mu_t = C_\mu \rho \frac{k^2}{\varepsilon} \tag{3}$$

$$S_{ij} = \frac{1}{2}\left(\frac{\partial \widetilde{\mu_i}}{\partial \widetilde{x_j}} + \frac{\partial \widetilde{\mu_j}}{\partial \widetilde{x_i}}\right) \tag{4}$$

In equation (3), C_μ is a model constant and ε is the dissipation of turbulent kinetic energy.

2.2.3. Heat transfer model

In our previous work, three different heat transfer models proposed by O'Rourke and Amsden [33], Han and Reitz [34], and Angelberger [35] were adopted to simulate the isobaric engine combustion process [36]. The results showed that the Angelberger model underpredicts the wall heat fluxes while the Han and Reitz model overpredicts the wall heat fluxes. Therefore, this work adopted the O'Rourke and Amsden model as the most accurate wall-function-based approach tested for predicting the heat transfer process in engine applications.

2.2.4. Computational mesh

Figure 4 shows the schematic of the computational domain. Since the piston shape is axisymmetric and the injector has 7 holes, a 51.4°-sector mesh was adopted to reduce computational expenses. Besides, the adaptive mesh refinement (AMR) module was activated, with which a finer mesh is generated dynamically where the computational field needs to be refined. A base mesh of 2.0 mm and an AMR scale of 3.0 were adopted, which generated the minimum mesh size of 0.25 mm. Based on the previous research [22, 37, 38], this mesh setup can achieve grid-convergence. The simulations started from the intake valve closing (IVC) timing (-160° crank angle after the top dead center (CA ATDC)) and ended at the exhaust valve opening (EVO) timing (140° CA ATDC), implying only closed-cycle modeling.

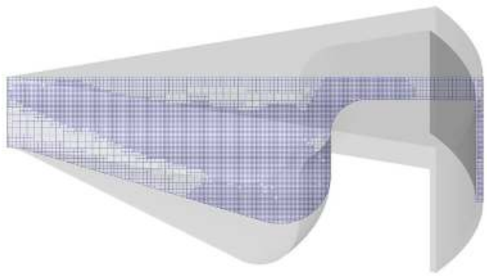

Fig. 4. Schematic of the computational domain.

2.2.5. Data-processing approach

A data-processing technique developed by Liu et al. [22, 23] was adopted to investigate the detailed chemical kinetics processes of the engine combustion heat release. In this method, the calculated 3D CFD results, together with the chemical kinetics mechanism, were taken as inputs. Instantaneous reactive source terms were computed by considering each cell as a perfectly stirred reactor [37, 39, 40]. For the analysis of the heat release features, the representative reaction which yielded the highest exothermic heat release rate (REXR) was used. More details about the method can be referred to [22, 23].

2.2.6. Parametric study cases

Swirl ratio (SW), spray angle (SA), and piston geometry are three of the most significant engine design parameters [41, 42]. Aa a result, a parametric modeling study was performed to analyze their effects on engine combustion performance and emissions, with the baseline case having the swirl ratio of 0, spray angle of 150°, and original piston geometry. Table 3 lists the parametric cases. For each studied parameter, the other parameters were the same as the baseline case. Figure 5(a) depicts the schematic of the five different spray angles, and Fig. 5(b) depicts the four different piston geometries, including the original (G1), shallow-type (G2), deep-type (G3), and toroidal-type (G4) geometries, respectively. Note that the chamber volume and squish height of the four geometries were kept the same to maintain a constant compression ratio.

Table 3. *Parametric cases.*

Parameter	Value
Swirl ratio	0, 1, 2, 3
Spray angle	160°, 150°, 140°, 130°, 120°
Geometry	G1, G2, G3, G4

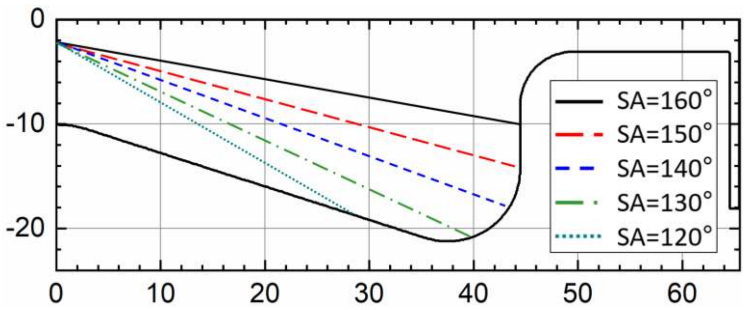

(a) Different spray angles.

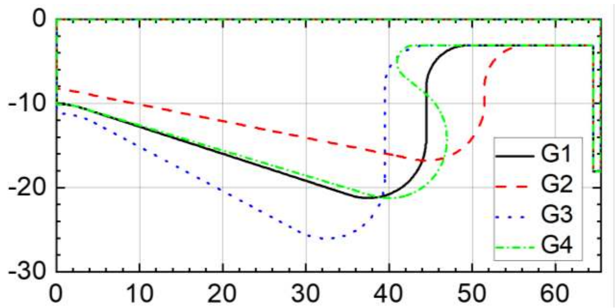

(b) Different piston geometries.

Fig. 5. *Schematics of the different (a) spray angles and (b) piston geometries. Axis unit: mm.*

3. Results and discussions

3.1. Comparison of the CDC and isobaric combustion

Figures 6(a) shows the experimental and predicted pressure and HRR profiles, while Fig. 6(b) shows the predicted energy distribution for the CDC and the 4-injection isobaric cases. Table 4 summarizes the experimental and predicted indicated thermal efficiency (ITE) and emissions. The simulated cases are able to predict the experimental results for both the CDC and isobaric combustion cases reasonably well. Only the THC and CO emissions are underpredicted, which may be attributed to the uncertainties in the adopted chemical kinetic mechanism and wall heat losses in the crevice region. Also, this work adopted n-heptane only to represent diesel combustion chemistry, which could also lead to the discrepancy. Note that, compared to the isobaric combustion mode, the CDC produces a significantly higher peak pressure. As a consequence, it is preferable to adopt the isobaric combustion mode for the DCEE concept from the durability and mechanical efficiency standpoints. Although the 4-injection isobaric case has a slightly lower ITE with its intrinsically late combustion phasing, the unused energy leaves the HP unit as an exhaust loss. The heat transfer loss, on the other hand, is reduced with the isobaric cycle. Recall that, unlike the heat transfer loss, the HP unit's exhaust energy can be further recovered by the LP unit of the DCEE, which should yield an overall higher thermal efficiency [19].

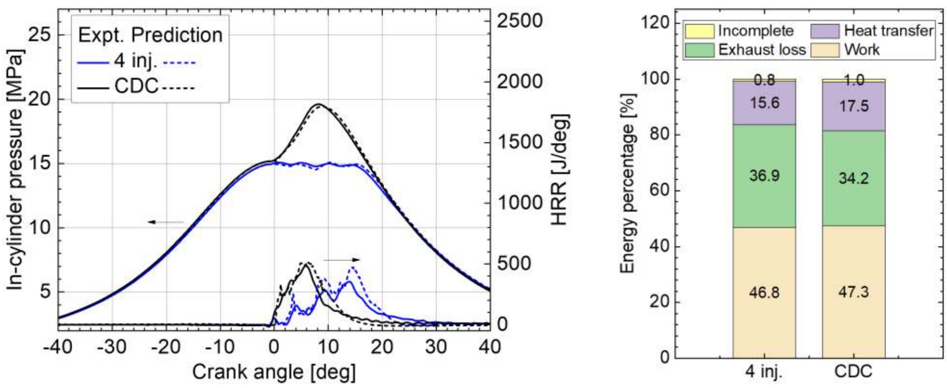

(a) (b)

Fig. 6. *Comparison of the (a) experimental and predicted pressure and HRR profiles and (b) predicted energy distributions for the CDC and 4 inj. cases.*

Table 4. *Experimental and predicted ITE and emissions for the CDC and 4 inj. cases.*

Parameters	Expt. (4 inj.)	Prediction (4 inj.)	Expt. (CDC)	Prediction (CDC)
ITE (%)	47.0	46.8	47.2	47.3
NOx (g/kW-h)	16.0	13.8	29.1	18.7

Soot (mg/kW-h)	0.49	0.58	0.71	0.60
CO (g/kW-h)	0.165	0.048	0.116	0.041
THC (g/kW-h)	0.166	0.0166	0.142	0.009

To further compare the heat release features between the CDC and isobaric combustion modes, Fig. 7 shows the predicted distributions of the HRR and the corresponding REXR regions for the CDC case and the 4-injection isobaric case, respectively. For both cases, the chemical ignitions (when the peak temperature reaches $(T_{ini} + T_{peak})/2$ [43]) are initiated just downstream of the injector tip, with the heat release dominated by the reaction R257 ($HCO+O_2=CO+HO_2$). At 2°CA ATDC, substantial heat is released at the peripheries of the fuel jet, where the reactions R233 ($OH+H_2=H+H_2O$) and R236 ($H+O_2(+M)=HO_2(+M)$) dominate. Note that until 6°CA ATDC, significant heat release is caused by the reactions R117 ($C_2H_4+H(+M)=C_2H_5(+M)$) and R207 ($CH_3+H(+M)=CH_4(+M)$) which occur inside the intensely reacting jet peripheries of the CDC case. This inhibits the rapid consumption of fuel and promotes the formation of soot precursors like acetylene [23, 44].

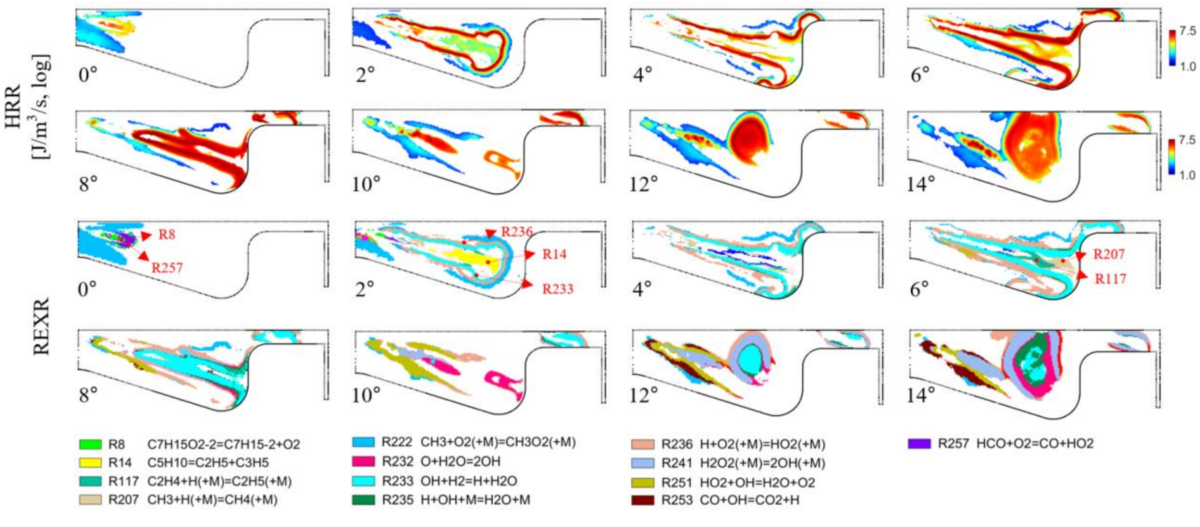

(a) CDC case.

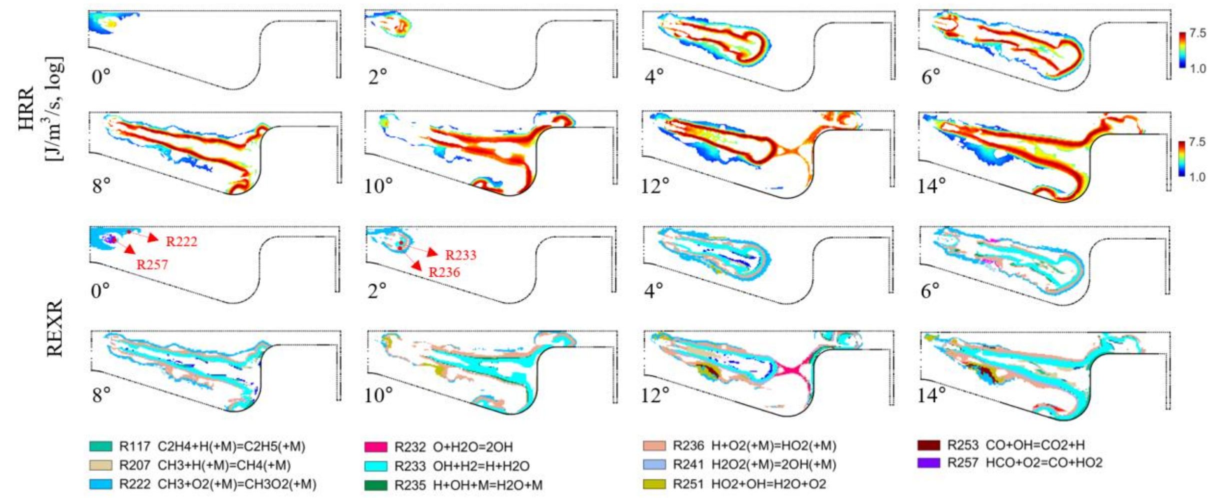

(b) 4 inj. case.

Fig. 7. *Predicted distributions of the HRR and REXR regions for the (a) CDC and (b) 4 inj. cases.*

3.2. Isobaric combustion at various engine loads

Figures 8(a) compares the experimental and predicted pressure and HRR profiles, whereas Fig. 8(b) compares the ITEs. To maintain constant combustion pressure, more fuel is injected in the later injection events. The simulations are able to capture the experimental results at various engine loads reasonably well, except that the thermal efficiency for the 2-injection isobaric case is over-predicted by about 6.5% points. This is due to the earlier combustion phasing and higher peak HRR predicted by the simulations. Note that at low engine loads (as in 2-injection case), the discrepancies between the experimental and predicted ITEs become amplified because of the normalization process involved; the pressure trace and HRR still show a very good match. With the increase of engine load, the thermal efficiency first grows, and then reduces. Peak thermal efficiencies are obtained with the 3- and 4-injection cases.

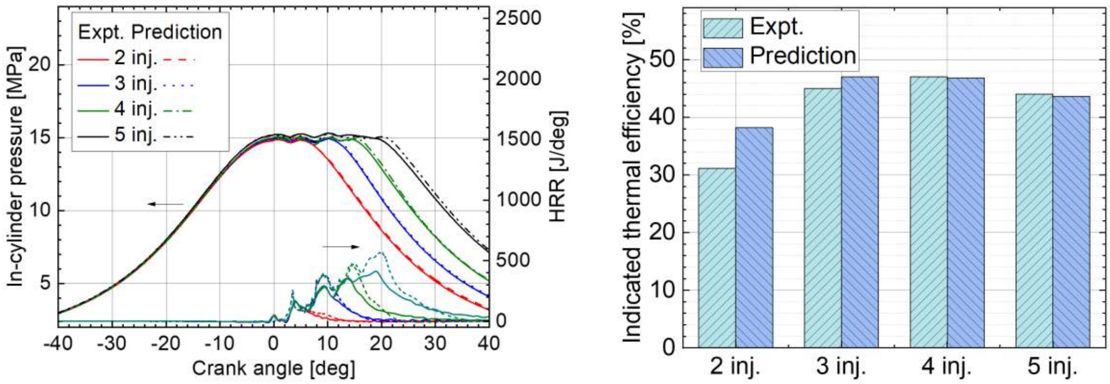

(a) In-cylinder pressure and HRR.

(b) Indicated thermal efficiency.

Fig. 8. *Comparison of the experimental and predicted (a) pressure and HRR profiles and (b) indicated thermal efficiency at various engine loads.*

Figures 9(a) and 9(b) compare the predicted energy distributions and average temperature profiles at various engine loads, respectively. At a higher engine load, the average temperature is increased due to the larger energy input, which results in higher exhaust temperature and a higher proportion of exhaust loss. Despite the higher average temperature at the higher engine load, the proportion of heat transfer loss is still reduced. The proportion of the exhaust loss, on the other hand, tends to increase with a higher load. The competition between heat transfer loss and exhaust loss leads to the initially increasing and later decreasing trend in thermal efficiency. Compared to the exhaust and heat transfer losses, the incomplete combustion loss remains at a low level (below 1%). Note that for the 5-injection isobaric case, the exhaust loss fraction is comparable to the useful work fraction. This emphasizes the importance of the use of exhaust energy recovery systems in modern engine concepts, such as the LP unit of the DCEE.

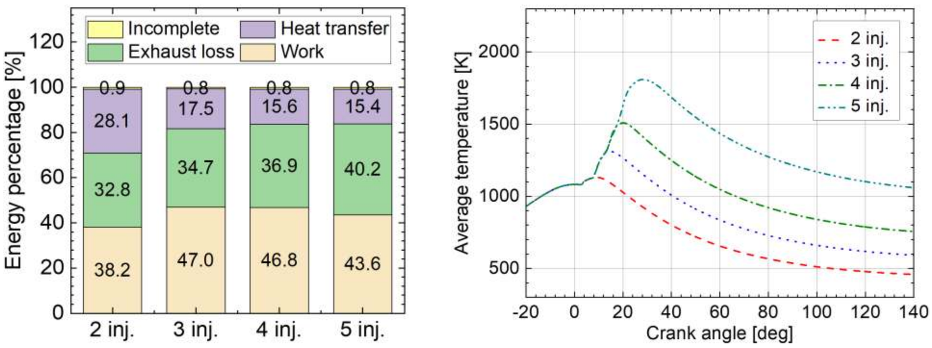

(a) Energy distributions. (b) Average temperature profiles.

Fig. 9. *Comparison of the predicted (a) energy distributions and (b) average temperature profiles at various engine loads.*

Figures 10 compares the experimental and predicted NOx, soot, CO, and THC emissions at various engine loads. Despite discrepancies in low-load cases, the trends are reasonably captured by the simulations. Note that the emissions are in a unit of g/kW-h, all of which show a declining trend with a higher load. The reductions of soot, CO, and THC emissions are primarily due to the higher combustion temperatures that enhance oxidation, while the declining of NOx in g/kW-h is due to the isobaric combustion restriction so that the injection timing must be delayed significantly. However, the absolute amount of NOx in volume fraction (ppm) grows with a higher load, owing to the longer combustion duration and larger high-temperature reaction zones. Therefore, the NOx/soot trade-off still exists when we adopt the units of ppm and g/m^3 for NOx and soot emissions, respectively.

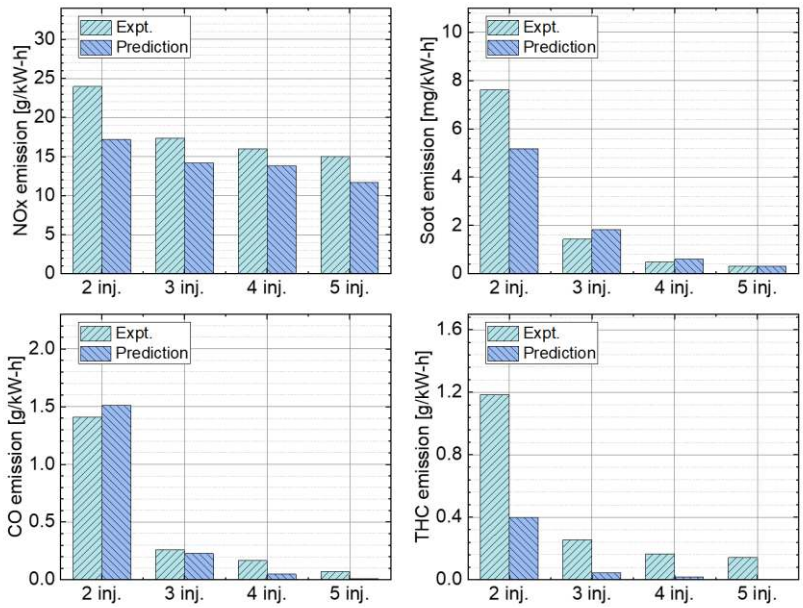

Fig. 10. *Comparison of the predicted and experimental NOx, soot, CO, and THC emissions at various engine loads.*

3.3. Parametric study on the isobaric combustion

3.3.1. Effect of swirl ratio

Figure 11 compares the predicted pressure and HRR profiles with different swirl ratios (SR) for the 4-injection isobaric cases. With a higher swirl ratio, in-cylinder pressure is lower before the top dead center (TDC), but higher after the second-injection combustion event. Figures 12(a) and 12(b) compare the average temperatures and air utilization profiles at different swirl ratios, respectively. Note that the lower percentage of $\phi > 1.5$ regions indicates better air utilization. It shows that a higher swirl ratio leads to a better air utilization rate. Therefore, the premixed HRR is higher with a higher swirl ratio, as shown in Fig. 11, which is especially apparent during the 3rd-and 4th-injection combustion events.

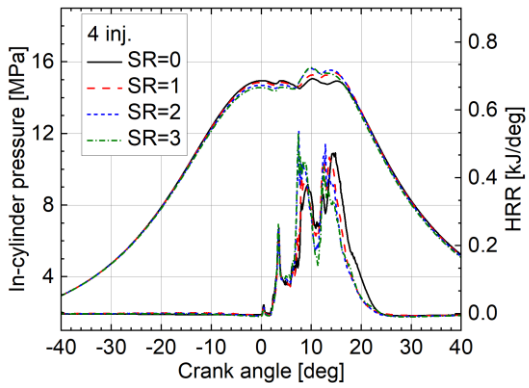

__Fig. 11.__ Comparison of the predicted pressure and HRR results with different swirl ratios for the 4 inj. cases.

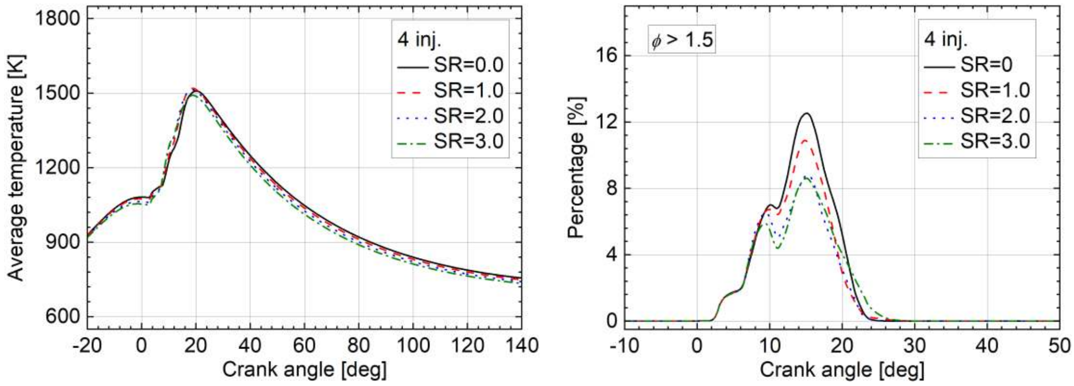

(a) Average temperature. (b) Air utilization profile.

__Fig. 12.__ Comparison of the predicted (a) average temperature and (b) air utilization profiles with different swirl ratios.

The higher swirl ratio also significantly affects the heat transfer process. Figure 13 compares the predicted evolutions of the heat transfer rate with different swirl ratios. A higher swirl ratio significantly enhances the heat transfer rate even before ignition. To further clarify this, Fig. 14 compares the predicted distributions of turbulent kinetic energy (TKE), temperature (T), and ϕ at different swirl ratios before the injection event (-4°CA ATDC). Note that a higher swirl ratio leads to a more tilting spray/flame plume. Besides, the higher swirl ratio increases the TKE, which leads to a higher heat transfer rate. Therefore, the more intense convection heat transfer process results in the lower near-wall and average temperatures before ignition.

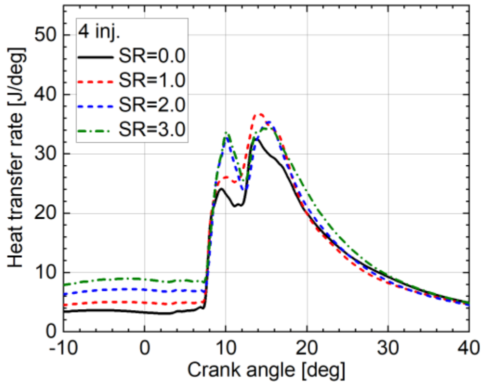

Fig. 13. *Comparison of the predicted evolutions of heat transfer rate at different swirl ratios.*

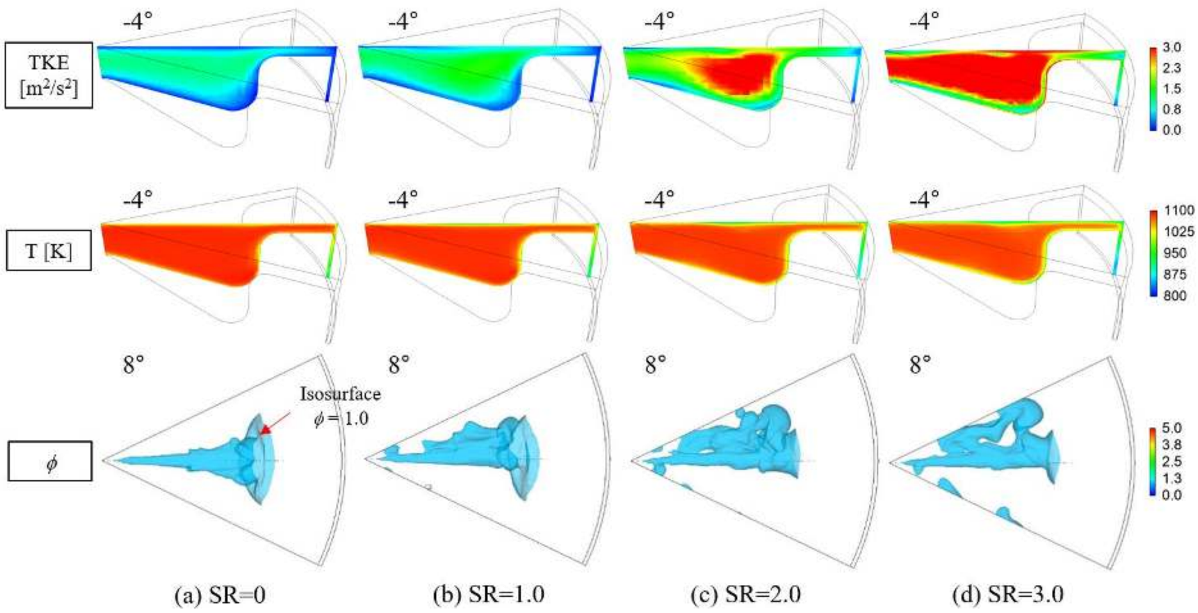

Fig. 14. *Comparison of the predicted distributions of turbulent kinetic energy (TKE), temperature (T), ϕ at different swirl ratios.*

Figure 15 compares the predicted energy distributions at various engine loads with different swirl ratios. A higher swirl ratio leads to a lower thermal efficiency, which is primarily due to the enhanced heat transfer loss. Besides, at different engine loads except the 5-injection case, exhaust loss fraction generally demonstrates a declining trend with a higher swirl ratio, which is owing to the faster combustion process and thus lower exhaust temperature as depicted in Fig. 12(a). Comparatively, the incomplete combustion loss fraction remains at a stably low level of about 1%.

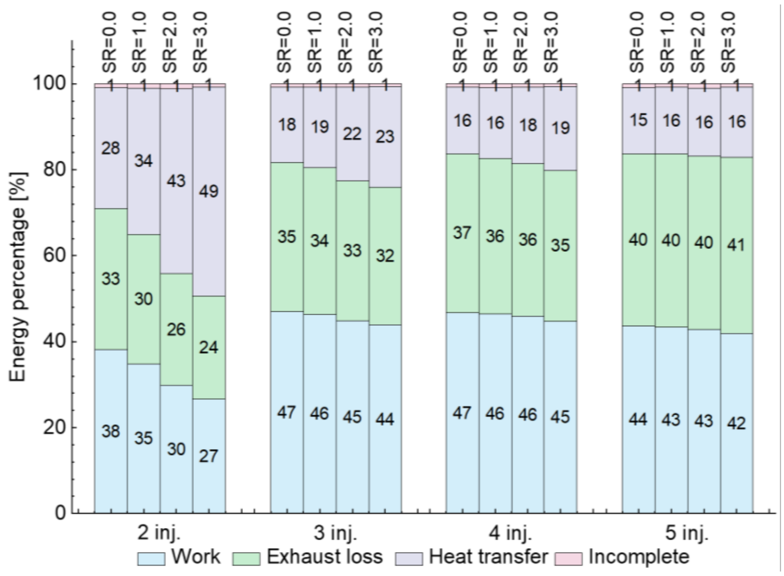

Fig. 15 *Comparison of the predicted energy distributions with different swirl ratios.*

Figure 16 compares the predicted emissions at various engine loads with different swirl ratios. With each swirl ratio, generally similar trends in the change of the emissions with different engine loads are observed, except that the soot, CO, and THC emissions are significantly higher for the 5-injection case at the swirl ratio of 3.0. This is primarily owing to the late combustion. Since a high swirl ratio stirs up the combustion region further from the upstream combustible fuel-air mixture, it delays the combustion and results in lower combustion temperature, as indicated by Fig. 12(a). Therefore, the oxidation rate is lower at this condition, which increases the soot, CO, and THC emissions.

For the 2-injection cases, all of the emissions in g/kW-h show a growing trend with a higher swirl ratio, owing to the joint effect of the lower work output and the premixed combustion process. For NOx emission, the 3-injection cases continue exhibiting a growing trend with a higher swirl ratio, but the higher-load cases demonstrate an overall declining trend, due to the lower temperature during the post-combustion period as depicted in Fig. 12 (a). For the other three kinds of emissions, the 3-and 4-injection cases both show a comparatively weak response to the higher swirl ratio. However, the 5-

injection cases show a growing trend since the higher swirl ratio has a more significant effect on the 5th-injection combustion period, which leads to a lower post-combustion temperature and thus lower oxidation rates of soot, CO, and HCs.

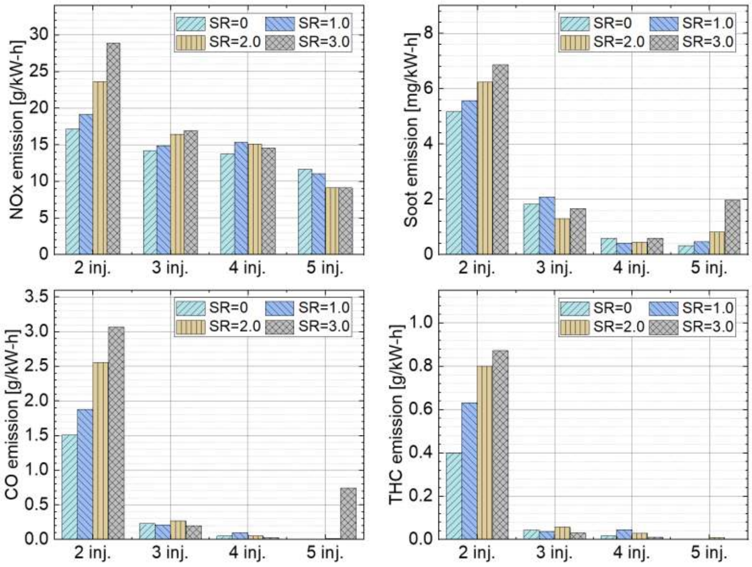

Fig. 16. *Comparison of the predicted NOx, soot, CO, and THC emissions with different swirl ratios.*

3.3.2. Effect of spray angle

Figure 17 compares the predicted pressure and HRR profiles with the different spray angles for the 4-injection isobaric cases. During the first and second injection events, combustion heat release is similar for all the cases. This is due to the low amount of injected fuel mass and thus a shorter spray penetration. As a result, the combustion is primarily confined within the chamber. However, different spray angles have a significant effect on the 3rd- and the 4th-injection combustion processes, owing to the significantly longer spray penetrations, hence more intense flame-wall interactions, which is clearly shown in Fig. 18. Note that a spray angle of 150° generates the highest combustion pressure during the 4th-injection combustion period, while spray angles of 160° and 120° generate the lowest combustion pressures. As seen in Fig. 18, cases with spray angles of 160° and 120° generate more combustion regions within the squish, which impairs the effective engine work and enhances the heat transfer loss.

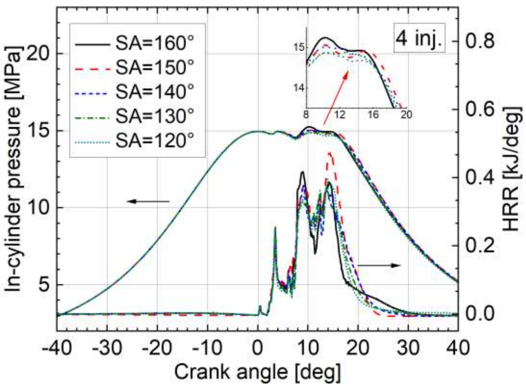

Fig. 17. *Comparison of the predicted pressure and HRR profiles with different spray angles for the 4 inj. cases.*

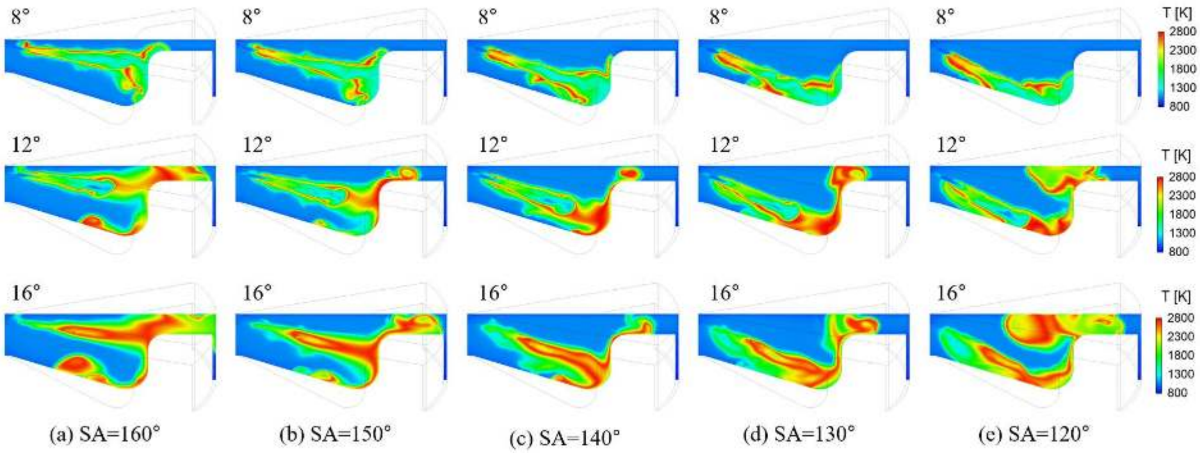

Fig. 18. *Comparison of the predicted distributions of T for the 4 inj. cases with different spray angles.*

Figure 19 compares the predicted energy distributions at various engine loads with different spray angles. As with the swirl ratio, the thermal efficiency follows the same trend with respect to the spray angle at different engine load conditions. An obvious firstly growing and then declining trend of thermal efficiency is observed as the spray angle is reduced from 160° to 120°. Peak thermal efficiencies are obtained with a spray angle of either 150° or 140°, primarily due to the more efficient combustion processes and lower heat transfer losses. Figures 20(a) and 20(b), respectively, compare the predicted average temperature and air utilization profiles for the 4-injection isobaric cases with different spray angles. The cases with spray angles of 150° and 140° yield the highest air utilization rates and combustion temperatures, which explain their higher thermal efficiencies.

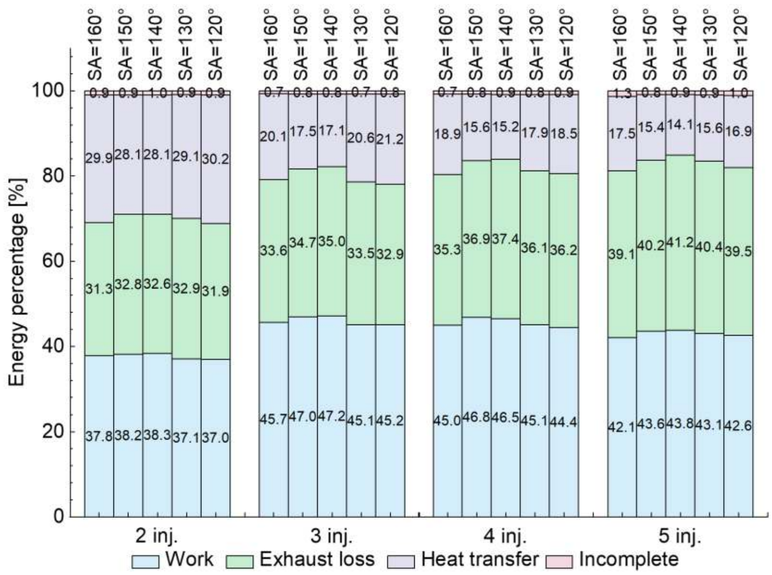

Fig. 19. *Comparison of the predicted energy distributions with different spray angles.*

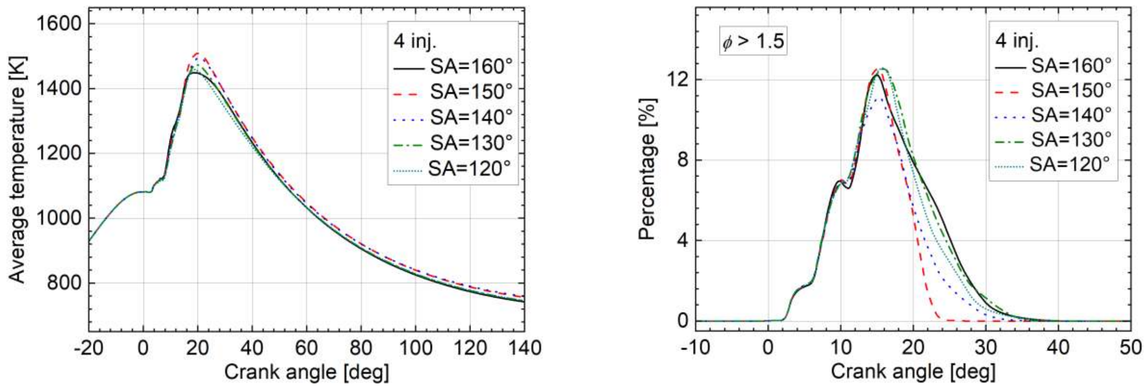

(a) Average temperature.

(b) Air utilization profile.

Fig. 20. *Comparison of the predicted (a) average temperature and (b) air utilization profiles with different spray angles.*

Figure 21 compares the predicted evolutions of the total heat transfer rate (HTR) and HTRs through the piston, cylinder head, and liner for the 4-injection isobaric cases with different spray angles. Clearly, the SA=140° case generates the lowest heat transfer loss, although it has a comparatively high average temperature, as seen in Fig. 20(a). Figures 21(b-d) show that the SA=140° case generates the lowest heat transfer loss through the liner, which means the combustion is well confined within the cylinder and squish regions, as seen in Fig. 18. Besides, it also generates comparatively low heat transfer losses through the piston and cylinder head simultaneously. These factors lead to the lowest heat transfer loss for the SA=140° case.

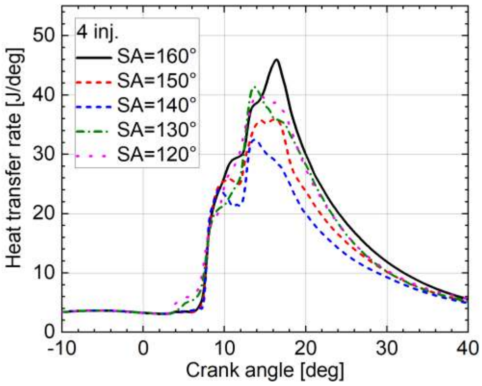

(a) Total HTR.

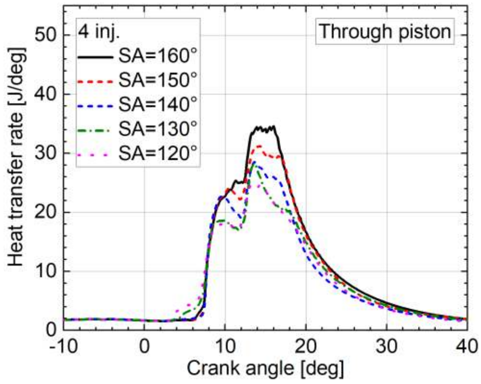

(b) HTR through piston.

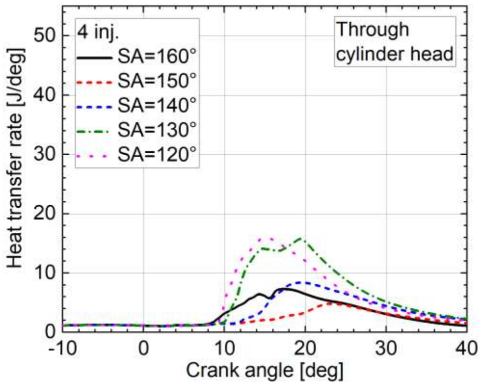

(c) HTR through cylinder head.

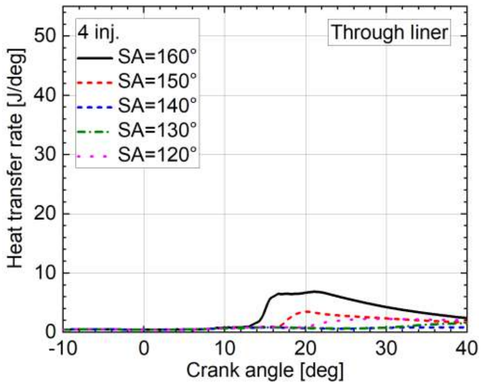

(d) HTR through liner.

Fig. 21. *Predicted evolutions of the (a) total HTR and HTR through (b) piston, (c) cylinder head, and (d) liner with different spray angles.*

Figure 22 compares the predicted NOx, soot, CO, and THC emissions at various engine loads with different spray angles. With each spray angle, different emissions generally show a declining trend with a higher load. Owing to the higher combustion temperature and air utilization rate (see Fig. 20), the cases with spray angles of 140° and 150° tend to generate higher NOx emissions and lower CO and THC emissions. Note that among the 5-injection isobaric cases, the case with a spray angle of 160° generates a significantly higher amount of soot, CO, and THC emissions. This is because a lot of fuel is injected into the squish region during the 5th injection event, which leads to poor air-fuel mixing characteristics and, hence, low oxidation rates of the pollutant species during the post-combustion period.

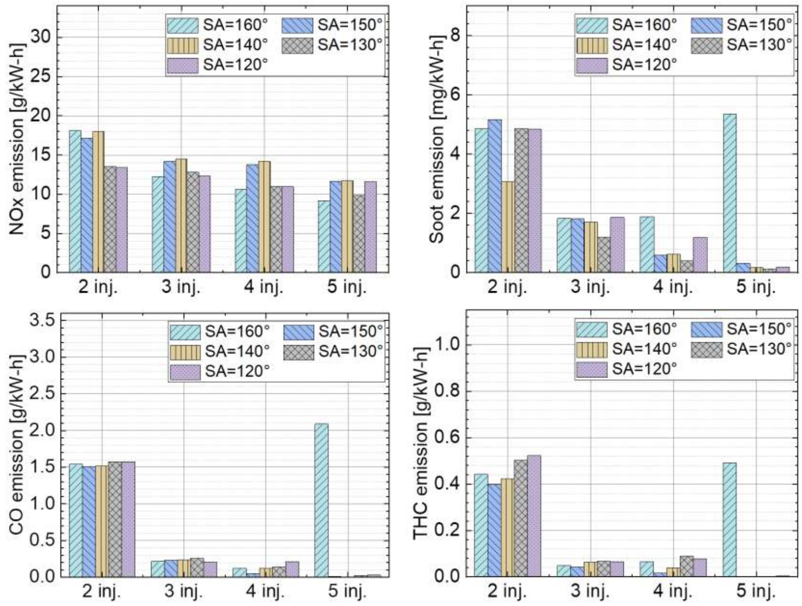

Fig. 22. *Comparison of the predicted NOx, soot, CO, and THC emissions with different spray angles.*

3.3.3. Effect of piston geometry

Figure 23 compares the predicted pressure and HRR profiles with the four different piston geometries for the 4-injection isobaric case. Comparatively, G1 and G2 show overall higher combustion pressures and HRRs, followed by G3, and then G4. For the 1st- and the 2nd-injection combustion events, different piston geometries have a negligible effect on the combustion process; however, there is a significant effect on the 3rd- and the 4th-injection combustion events, which is clearly shown in Fig. 24. Comparatively, G2 generates the longest spray-flame plume due to the longest inner piston radius; G3 generates the most combustion regions within the piston due to the deeper piston design; while G4 generates a spray-flame plume that is primarily confined within the combustion chamber, which, however, leads to the overall lower combustion temperature.

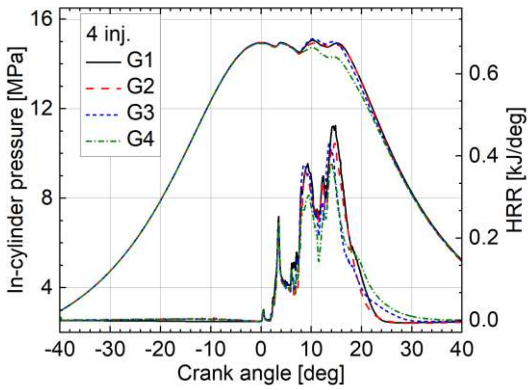

Fig. 23. *Comparison of the predicted pressure and HRR profiles with four piston geometries for the 4 inj. cases.*

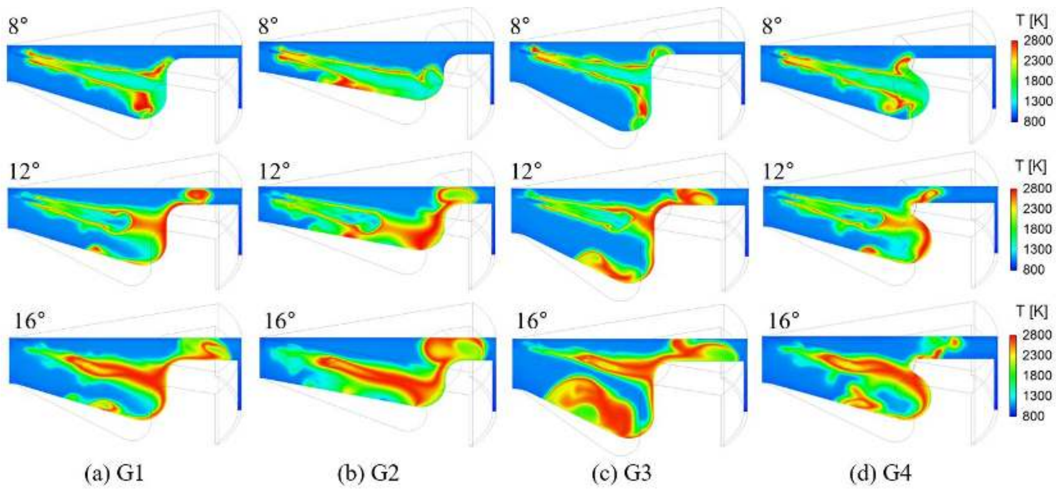

Fig. 24. *Comparison of the predicted distributions of T with four piston geometries.*

Figure 25 compares the predicted energy distributions at various engine loads with different piston geometries. With each piston geometry, thermal efficiency at a higher load demonstrates a firstly growing and then declining trend. For the 2-injection isobaric cases, G2 generates the highest thermal efficiencies among four piston geometries, primarily due to the lowest heat transfer loss. For the 3-, 4-, and 5-injection isobaric cases, however, G1 generates the highest thermal efficiencies, owing to the low heat transfer and exhaust losses together.

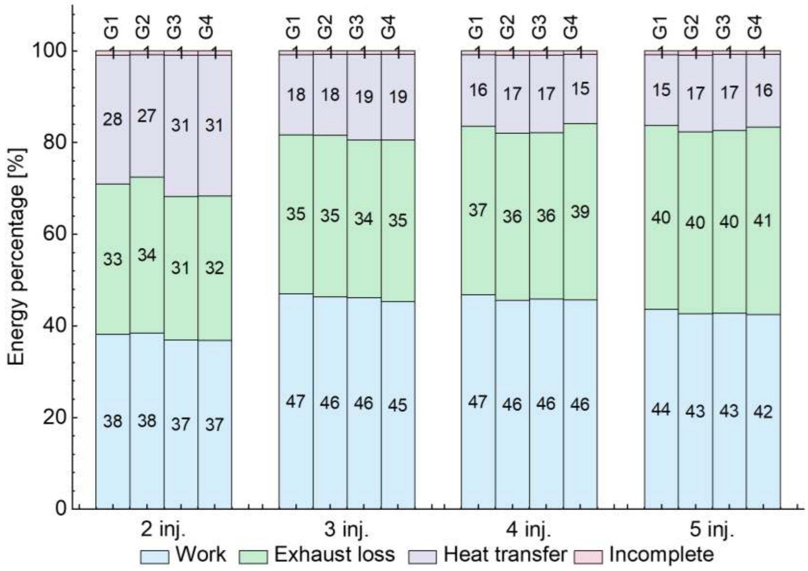

Fig. 25. *Comparison of the predicted energy distributions with four piston geometries.*

Note that for the 4- and 5-injection isobaric cases, although G4 yields a significantly lower combustion pressure during the 3rd- and the 4th-injection combustion periods, it eventually generates similar thermal efficiencies as G2 and G3. To clarify this, Figs. 26(a) and 26(b) compare the predicted average temperature and air utilization profiles for the 4-injection isobaric cases. It reveals that the lower HRR in the G4 case is primarily due to the lower air-utilization during the 4th-injection combustion period. Therefore, G4 yields a lower average temperature, which results in a lower heat transfer loss. This explains its comparable thermal efficiency with G2 and G3.

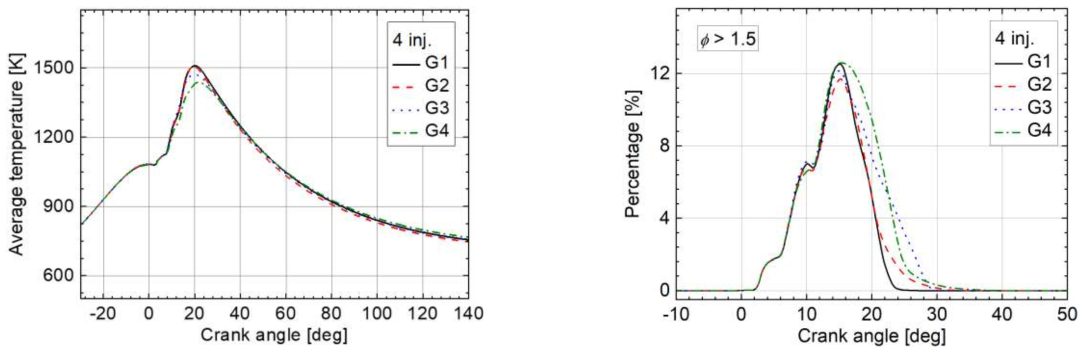

(a) Average temperature.

(b) Air utilization profile.

Fig. 26. *Comparison of the predicted (a) average temperature and (b) air utilization profiles with four piston geometries.*

Figure 27 compares the predicted NOx, soot, CO, and THC emissions with different piston geometries. Still, with each piston geometry, each pollutant species demonstrates a declining trend with a higher engine load. Since the formation of NOx is closely related to combustion temperature, G1 tends to generate higher NOx emissions compared to the other piston geometries due to the generally higher combustion temperature, as seen in Fig. 26(a). Note that for the 3-, 4-, and 5-injection isobaric cases, there is a declining trend in NOx emissions when changing the piston geometry from G2 to G4, owing to the declining trend in combustion temperature.

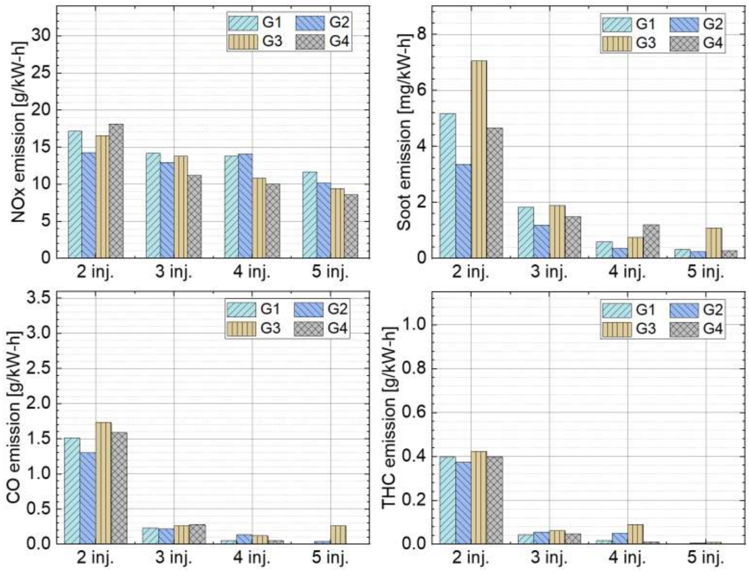

Fig. 27. *Comparison of the predicted NOx, soot, CO, and THC emissions with four piston geometries.*

Emissions of soot, CO, and THC at various engine loads demonstrate a more complicated behavior. Figure 28 compares the predicted evolutions for soot, CO, and C_2H_4 (ethylene) with different piston geometries. C_2H_4 is used because it is one of the primary compositions of THC emissions [45]. Note that before the 3rd-injection combustion periods, all pollutants show similar results regardless of the piston geometry. After that, significant discrepancies are observed, since different piston geometries start playing a more important role in the in-cylinder flow and fuel-air mixing processes.

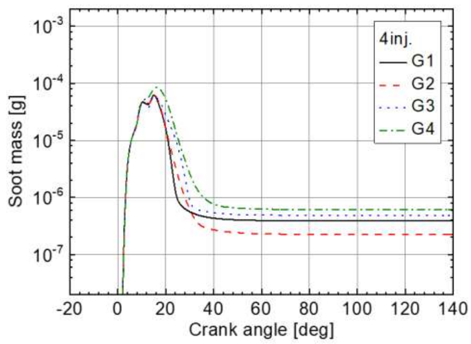

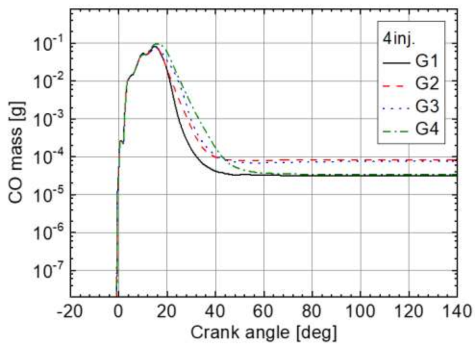

(a) Soot. (b) CO.

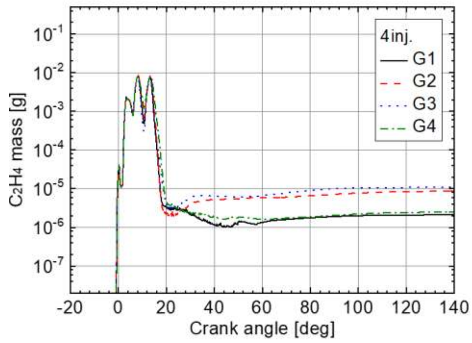

(c) C_2H_4.

Fig. 28. *Comparison of predicted evolutions of soot, CO, and C_2H_4 for the 4 inj. cases with four piston geometries.*

3.3.4. Summary

To summarize the effects of swirl ratio, spray angle, and piston geometry on the efficiency and emissions of the isobaric combustion mode, two merit functions are defined with the baseline case (SW=0, SA=150°, and G1) as a reference [46],

$$Merit_{ITE} = 100 * (\frac{ITE}{ITE_{ori}} - 1) \quad (5)$$

$$Merit_{emission} = 100 * [(\frac{NO_x}{NO_{x_{ori}}} - 1) + 0.1 * \left(\frac{SOOT}{SOOT_{ori}} + \frac{CO}{CO_{ori}} - 2\right) + 0.01 * (\frac{THC}{THC_{ori}} - 1)] \quad (6)$$

Besides, the merit value at each engine load is multiplied by a weight factor based on the total injected mass and then summed up. The weight factor is calculated by,

$$W_i = \frac{m_i}{\sum m_i} \quad (7)$$

Figures 29(a) and 29(b) summarize the calculated $Merit_{ITE}$ and $Merit_{emission}$ for the isobaric combustion cases. The adoption of a higher swirl ratio or a different piston geometry than the original one has a negative effect on the thermal efficiency, and hence, the fuel economy. A peak ITE is obtained with a spray angle of 140°, with a 0.1% improvement compared to the baseline case. On the other hand, a higher swirl ratio increases engine-out emissions, while spray angles of 140° and 130° and piston geometries of G3 and G4 all reduce engine-out emissions. In summary, considering both the fuel economy and emission factors, the original piston shape (G1) with a spray angle of 140° and a swirl ratio of 0 yields the best performance for the isobaric combustion mode.

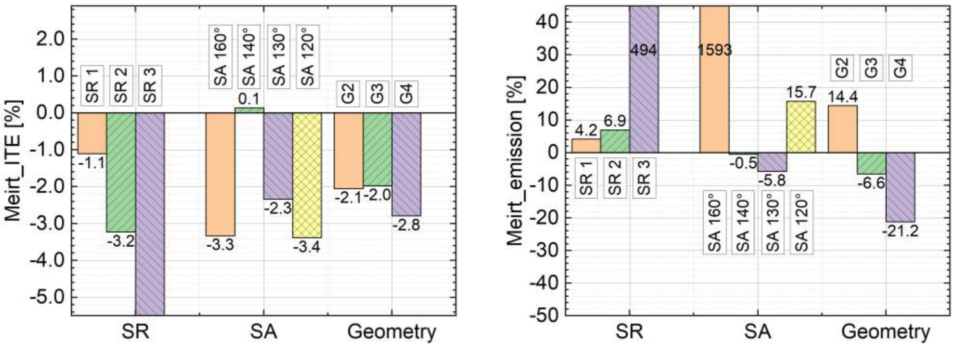

(a) $Merit_{ITE}$. (b) $Merit_{emission}$.

Fig. 29. *Summary of the predicted (a) $Merit_{ITE}$ and (b) $Merit_{emission}$ for the isobaric combustion cases.*

4. Conclusions and future work

This work numerically investigated the isobaric combustion mode using a three-dimensional modeling approach. An in-house data-processing method was utilized to understand and compare the detailed combustion features of the conventional diesel and isobaric combustion modes. Besides, the effects of swirl ratio, spray angle, and piston geometries on the engine combustion performance and emissions were investigated at various engine loads. The conclusions of this work are summarized as follows:

(1) The isobaric combustion mode generated a significantly lower peak pressure but a similar

thermal efficiency compared to the conventional diesel combustion mode, which is more preferable for the double compression expansion engine concept.

(2) A higher swirl ratio led to the higher turbulent kinetic energy and air utilization rate, but it also resulted in the higher heat transfer loss and thus the lower thermal efficiency.

(3) Cases with spray angles of 140° and 150° generated the higher thermal efficiencies owing to the more efficient combustion processes and lower heat transfer losses.

(4) Different piston geometries demonstrated a significant impact on the post-combustion period at a higher engine load, with original piston shape generally yielding the highest thermal efficiency.

(5) The original piston shape with a spray angle of 140° and a swirl ratio of 0 yields the best performance for the isobaric combustion mode.

This work primarily focused on three parameters (swirl ratio, spray angle, and piston geometry) with the start of injection timings unchanged. In the future, more studies will be performed by optimizing the injector setup, injection strategy, and piston geometry simultaneously. Considering the multiple-parameter target, the machine learning method may be necessary.

Acknowledgments

The paper is based upon work supported by Saudi Aramco Research and Development Center FUELCOM3 program under Master Research Agreement Number 6600024505/01. FUELCOM (Fuel Combustion for Advanced Engines) is a collaborative research undertaking between Saudi Aramco and KAUST intended to address the fundamental aspects of hydrocarbon fuel combustion in engines, and develop fuel/engine design tools suitable for advanced combustion modes. The computational simulations were performed using the clusters at KAUST Supercomputing Laboratory. The authors also thank Convergent Science Inc. for providing the CONVERGE licenses.

References

[1] Reitz R.D., Ogawa H., Payri R., Fansler T., Kokjohn S., Moriyoshi Y., Agarwal A., Arcoumanis D., Assanis D., Bae C., Boulouchos K., Canakci M., Curran S., Denbratt I., Gavaises M., Guenthner M., Hasse C., Huang Z., Ishiyama T., Johansson B., Johnson T., Kalghatgi G., Koike M., Kong S., Leipertz A., Miles P., Novella R., Onorati A., Richter M., Shuai S., Siebers D., Su W., Trujillo M., Uchida N., Vaglieco B.M., Wagner R., Zhao H. IJER editorial: The future of the internal combustion engine. Int. J. Engine Res. 2020; 21(1): 3-10.

[2] Desantes J.M., Garcia-Oliver J.M., Novella R., Pachano L. A numerical study of the effect of nozzle diameter on diesel combustion ignition and flame stabilization. Int. J. Engine Res. 2020; 21(1): 101-121.

[3] Singh R., Han T., Fatouraie M., Mansfield A., Wooldridge M., Boehman A. Influence of fuel injection strategies on efficiency and particulate emissions of gasoline and ethanol blends in a turbocharged multi-cylinder direct injection engine. Int. J. Engine Res. 2019; 0(0): 1468087419838393.

[4] Tan J.Y., Bonatesta F., Ng H.K., Gan S. Developments in computational fluid dynamics modelling of gasoline direct injection engine combustion and soot emission with chemical kinetic modelling. Appl. Therm. Eng. 2016; 107: 936-959.

[5] Lam N., Tuner M., Tunestal P., Andersson A., Lundgren S., Johansson B. Double compression expansion engine concepts: A path to high efficiency. SAE Technical Paper 2015; 2015-01-1260.

[6] Powell T., O'Donnell R., Hoffman M., Filipi Z., Jordan E.H., Kumar R., Killingsworth N.J. Experimental investigation of the relationship between thermal barrier coating structured porosity and homogeneous charge compression ignition engine combustion. Int. J. Engine Res. 2019; 0(0): 1468087419843752.

[7] Guan W., Pedrozo V.B., Zhao H., Ban Z., Lin T. Miller cycle combined with exhaust gas recirculation and post–fuel injection for emissions and exhaust gas temperature control of a heavy-duty diesel engine. Int. J. Engine Res. 2020; 21(8): 1381-1397.

[8] Yao M., Chen Z., Zheng Z., Zhang B., Xing Y. Study on the controlling strategies of homogeneous charge compression ignition combustion with fuel of dimethyl ether and methanol. Fuel 2006; 85(14-15): 2046-2056.

[9] Yao M., Zheng Z., Liu H. Progress and recent trends in homogeneous charge compression ignition (HCCI) engines. Prog. Energy Combust. Sci. 2009; 35(5): 398-437.

[10] Chen Z., Yao M., Zheng Z., Zhang Q. Experimental and numerical study of methanol/dimethyl ether dual-fuel compound combustion. Energy Fuels 2009; 23(5): 2719-2730.

[11] Noehre C., Andersson M., Johansson B., Hultqvist A. Characterization of partially premixed combustion. SAE Technical Paper 2006; 2006-01-3412.

[12] Hildingsson L., Kalghatgi G., Tait N., Johansson B., Harrison A. Fuel octane effects in the partially premixed combustion regime in compression ignition engines SAE Technical Paper 2009; 2009-01-2648.

[13] Yang B., Yao M., Cheng W.K., Zheng Z., Yue L. Regulated and unregulated emissions from a compression ignition engine under low temperature combustion fuelled with gasoline and n-butanol/gasoline blends. Fuel 2014; 120: 163-170.

[14] Liu X., Wang H., Wang X., Zheng Z., Yao M. Experimental and modelling investigations of the diesel surrogate fuels in direct injection compression ignition combustion. Appl. Energy 2017; 189: 187-200.

[15] Lapuerta M., Ramos Á., Fernández-Rodríguez D., González-García I. High-pressure versus low-

pressure exhaust gas recirculation in a Euro 6 diesel engine with lean-NOx trap: Effectiveness to reduce NOx emissions. Int. J. Engine Res. 2019; 20(1): 155-163.

[16] Allen C.M., Joshi M.C., Gosala D.B., Shaver G.M., Farrell L., McCarthy J. Experimental assessment of diesel engine cylinder deactivation performance during low-load transient operations. Int. J. Engine Res. 2019; 0(0): 1468087419857597.

[17] Lam N., Tunestal P., Andersson A. Simulation of system brake efficiency in a Double Compression-Expansion Engine-Concept (DCEE) based on experimental combustion data. SAE Technical Paper 2019; 2019-01-0073.

[18] Rafig Babayev M.B.H., VS Bhavani Shankar, Bassam Aljohani, Bengt Johansson. Injection strategies for isobaric combustion. SAE Technical Paper 2019; 2019-01-2267.

[19] Lam N., Andersson A., Tunestal P. Double compression expansion engine concepts: Efficiency analysis over a load range. SAE Technical Paper 2018; 2018-01-0886.

[20] Okamoto T., Uchida N. New concept for overcoming the trade-off between thermal efficiency, each loss and exhaust emissions in a heavy duty diesel engine. SAE Technical Paper 2016; 2016-01-0729.

[21] Babayev R., Ben Houidi M., Andersson A., Johansson B. Isobaric combustion: A potential path to high efficiency, in combination with the double compression expansion engine (DCEE) concept. SAE Technical Paper 2019; 2019-01-0085.

[22] Liu X., Kokjohn S., Wang H., Yao M. A comparative numerical investigation of reactivity controlled compression ignition combustion using Large Eddy Simulation and Reynolds-Averaged Navier-Stokes approaches. Fuel 2019; 257: 116023.

[23] Liu X., Wang H., Zhang Y., Yao M. A numerical investigation on the chemical kinetics process of

a reacting n-dodecane spray flame under compression ignition combustion condition. Energy Fuels 2019; 33(11): 11899-11912.

[24] Richards K., Senecal P., Pomraning E., CONVERGE (v2.3), Madison (WI): Convergent Science.

[25] Senecal P.K., Pomraning E., Richards K.J., Som S. An investigation of grid convergence for spray simulations using an LES turbulence model. SAE Technical Paper 2013; 2013-01-1083.

[26] Ricart L.M., Reitz R.D., Dec J.E. Comparisons of diesel spray liquid penetration and vapor fuel distributions with in-cylinder optical measurements. J. Eng. Gas Turbines Power 2000; 122(4): 588-595.

[27] Schmidt D.P., Rutland C.J. A new droplet collision algorithm. J. Comput. Phys. 2000; 164(1): 62-80.

[28] Froessling N. Evaporation, heat transfer, and velocity distribution in two-dimensional and rotationally symmetrical laminar boundary-layer flow. N.A.C.A. 1956; 168: AD-B189.

[29] Senecal P.K., Pomraning E., Richards K.J., Briggs T.E., Choi C.Y., McDavid R.M., Patterson M.A. Multi-dimensional modeling of direct-injection diesel spray liquid length and flame lift-off length using CFD and parallel detailed chemistry. SAE Technical Paper 2003; 2003-01-1043.

[30] Wang H., Yao M., Yue Z., Jia M., Reitz R.D. A reduced toluene reference fuel chemical kinetic mechanism for combustion and polycyclic-aromatic hydrocarbon predictions. Combust. Flame 2015; 162(6): 2390-2404.

[31] Som S. Development and validation of spray models for investigating diesel engine combustion and emissions. Ph.D. thesis, University of Illinois at Chicago, 2009.

[32] Han Z., Reitz R.D. Turbulence modeling of internal combustion engines using RNG κ-ε models. Combust. Sci. Technol. 1995; 106(4-6): 267-295.

[33] Amsden A.A., KIVA3V, Rel.2, Improvements to KIVA3V, LA Report, LA-UR-99-915, Los Alamos National Lab., 1999.

[34] Han Z., Reitz R.D. A temperature wall function formulation for variable-density turbulent flows with application to engine convective heat transfer modeling. Int. J. Heat Mass Transfer 1997; 40(3): 613-625.

[35] Angelberger C., Poinsot T., Delhay B. Improving near-wall combustion and wall heat transfer modeling in SI engine computations. SAE Technical Paper 1997; 972881.

[36] Aljabri H.H., Babayev R., Liu X., Badra J., Johansson B., Im H.G. Validation of computational models for isobaric combustion engines. SAE Technical Paper 2020; 2020-01-0806.

[37] Liu X., Kokjohn S., Li Y., Wang H., Li H., Yao M. A numerical investigation of the combustion kinetics of reactivity controlled compression ignition (RCCI) combustion in an optical engine. Fuel 2019; 241: 753-766.

[38] Senecal P.K., Pomraning E., Richards K.J., Som S. Grid-convergent spray models for internal combustion engine computational fluid dynamics simulations. J. Energy Resour. Technol. 2013; 136(1): 012204.

[39] Li Y., Li H., Guo H. A numerical investigation on NO2 formation reaction pathway in a natural gas-diesel dual fuel engine. Combust. Flame 2018; 190: 337-348.

[40] Tang Q., Liu X., Liu H., Wang H., Yao M. Investigation on the dual-fuel active-thermal atmosphere combustion strategy based on optical diagnostics and numerical simulations. Fuel 2020; 276: 118023.

[41] Fridriksson H.S., Tuner M., Andersson O., Sunden B., Persson H., Ljungqvist M. Effect of piston bowl shape and swirl ratio on engine heat transfer in a light-duty diesel engine. SAE Technical Paper 2014; 2014-01-1141.

[42] Lechner G.A., Jacobs T.J., Chryssakis C.A., Assanis D.N., Siewert R.M. Evaluation of a narrow spray cone angle, advanced injection timing strategy to achieve partially premixed compression ignition combustion in a diesel engine SAE Technical Paper 2005; 2005-01-0167.

[43] Zhao W., Wei H., Jia M., Lu Z., Luo K.H., Chen R., Zhou L. Flame-spray interaction and combustion features in split-injection spray flames under diesel engine-like conditions. Combust. Flame 2019; 210: 204-221.

[44] Wang H., Frenklach M. A detailed kinetic modeling study of aromatics formation in laminar premixed acetylene and ethylene flames. Combust. Flame 1997; 110(1): 173-221.

[45] Choi B., Jiang X., Kim Y.K., Jung G., Lee C., Choi I., Song C.S. Effect of diesel fuel blend with n-butanol on the emission of a turbocharged common rail direct injection diesel engine. Appl. Energy 2015; 146: 20-28.

[46] Pei Y., Pal P., Zhang Y., Traver M., Cleary D., Futterer C., Brenner M., Probst D., Som S. CFD-guided gombustion system optimization of a gasoline range fuel in a heavy-duty compression ignition engine using automatic piston geometry generation and a supercomputer. SAE Technical Paper 2019; 2019-01-0001.